Multiscale assimilation of Advanced Microwave Scanning Radiometer–EOS snow water equivalent and Moderate Resolution Imaging Spectroradiometer snow cover fraction observations in northern Colorado

Gabriëlle J. M. De Lannoy,[1,2] Rolf H. Reichle,[2] Kristi R. Arsenault,[3] Paul R. Houser,[3] Sujay Kumar,[2] Niko E. C. Verhoest,[1] and Valentijn R. N. Pauwels[1]

[1]   Eight years (2002–2010) of Advanced Microwave Scanning Radiometer–EOS (AMSR-E) snow water equivalent (SWE) retrievals and Moderate Resolution Imaging Spectroradiometer (MODIS) snow cover fraction (SCF) observations are assimilated separately or jointly into the Noah land surface model over a domain in Northern Colorado. A multiscale ensemble Kalman filter (EnKF) is used, supplemented with a rule-based update. The satellite data are either left unscaled or are scaled for anomaly assimilation. The results are validated against in situ observations at 14 high-elevation Snowpack Telemetry (SNOTEL) sites with typically deep snow and at 4 lower-elevation Cooperative Observer Program (COOP) sites. Assimilation of coarse-scale AMSR-E SWE and fine-scale MODIS SCF observations both result in realistic spatial SWE patterns. At COOP sites with shallow snowpacks, AMSR-E SWE and MODIS SCF data assimilation are beneficial separately, and joint SWE and SCF assimilation yields significantly improved root-mean-square error and correlation values for scaled and unscaled data assimilation. In areas of deep snow where the SNOTEL sites are located, however, AMSR-E retrievals are typically biased low and assimilation without prior scaling leads to degraded SWE estimates. Anomaly SWE assimilation could not improve the interannual SWE variations in the assimilation results because the AMSR-E retrievals lack realistic interannual variability in deep snowpacks. SCF assimilation has only a marginal impact at the SNOTEL locations because these sites experience extended periods of near-complete snow cover. Across all sites, SCF assimilation improves the timing of the onset of the snow season but without a net improvement of SWE amounts.

Citation: De Lannoy, G. J. M., R. H. Reichle, K. R. Arsenault, P. R. Houser, S. Kumar, N. E. C. Verhoest, and V. R. N. Pauwels (2012), Multiscale assimilation of Advanced Microwave Scanning Radiometer–EOS snow water equivalent and Moderate Resolution Imaging Spectroradiometer snow cover fraction observations in northern Colorado, *Water Resour. Res.*, *48*, W01522, doi:10.1029/2011WR010588.

1.   Introduction

[2]   Snowmelt runoff is of major importance to summer water supplies [*Barnett et al.*, 2008; *Dyer*, 2008], and plays a considerable role in flood events [*Perry*, 2000] in midlatitudes and northern latitudes. Snow alters the interface between the atmosphere and the land surface through its higher albedo and lower roughness compared to snow-free conditions, and by thermally insulating the soil from the atmosphere. Consequently, the presence of snow strongly affects the land surface water and energy balance, weather [*Jin and Miller*, 2007; *Gong et al.*, 2004] and climate [*Bamzai and Shukla*, 1999; *Cohen and Entekhabi*, 1999; *Yang et al.*, 2001]. Moreover, snow has a high spatial and temporal variability, which is very sensitive to global change [*Déry and Wood*, 2006; *Mote et al.*, 2005; *Brown and Mote*, 2009; *Brown et al.*, 2010; *Brown and Robinson*, 2011].

[3]   In situ snow observations are collected at numerous meteorological stations (e.g., the National Oceanic and Atmospheric Administration Cooperative Observer Program (COOP) station network), by special snow monitoring networks (e.g., the Natural Resources Conservation Service (NRCS) Snowpack Telemetry (SNOTEL) network) and during intensive field campaigns. Moreover, Earth observing satellites provide global direct or indirect estimates of the snow state, but with limited accuracy and discontinuous spatio-temporal coverage. In addition, numerical integration of surface meteorological estimates from global atmospheric data assimilation systems into a land surface model (LSM) provides continuous estimates of the land surface

[1]Laboratory of Hydrology and Water Management, Ghent University, Ghent, Belgium.
[2]NASA Goddard Space Flight Center, Greenbelt, Maryland, USA.
[3]Department of Atmospheric, Oceanic and Earth Sciences, George Mason University, Calverton, Maryland, USA.

state, including snow. However, the representation of snow processes in LSMs is far from perfect [*Slater et al.*, 2001; *Rutter et al.*, 2009; *Dutra et al.*, 2010], and the assimilation of snow observations into an LSM may provide a more accurate estimate of snow conditions at spatial scales down to 1 km. Several studies report the assimilation of in situ snow observations [*Liston et al.*, 1999; *Slater and Clark*, 2006; *Liston and Hiemstra*, 2008], including for operational applications (e.g., National Operational Hydrologic Remote Sensing Center [*Barrett*, 2003], Canadian Meteorological Centre [*Brasnett*, 1999], European Centre for Medium-Range Weather Forecasting [*Drusch et al.*, 2004]). In the following, we will focus on satellite snow data assimilation.

[4] Various types of satellite observations can be used to discern snow covered and snow free areas. Sources include visible and near-infrared measurements such as those from the Moderate Resolution Imaging Spectroradiometer (MODIS, 2000 to present) on the Terra and Aqua platforms, the Landsat Thematic Mapper (TM, 1982 to present) and the advanced very high resolution radiometer (AVHRR, 1978 to present). While these data are fairly accurate, they come with a number of limitations, including the inability of these sensors to see through clouds [*Hall and Riggs*, 2007].

[5] Moreover, satellite-based snow cover fraction (SCF) products only provide a partial estimate of the snow state, namely snow cover, whereas hydrologic modeling is mostly concerned with estimating snow water equivalent (SWE; that is, snow mass). Snow depletion curves are often used to relate SCF to SWE [*Essery and Pomeroy*, 2004]. Observed snow cover maps can be used to parameterize these curves in a hydrological model [*Déry et al.*, 2005; *Lee et al.*, 2005]. Alternatively, techniques for SWE reconstruction after the end of the snow season have been proposed [*Durand et al.*, 2008a, 2008b; *Molotch*, 2009]. Dynamic assimilation of snow cover observations to update the state variables of a hydrologic model has been explored through rule-based "direct insertion" algorithms [*Rodell and Houser*, 2004; *Hall et al.*, 2010], nudging forcing fields toward likely precursors of the observed snow cover area [*Zaitchik and Rodell*, 2009] and ensemble Kalman filter (EnKF) approaches [*Clark et al.*, 2006; *Su et al.*, 2008]. Visible or near-infrared observations do not allow assimilation updates under cloudy conditions and the updates are typically affected by the uncertainties associated with the estimation of SWE for a given binary snow presence or a fractional snow cover (snow depletion curves). In this paper, we assimilate fine-scale satellite-based snow cover fraction observations instead of the binary presence or absence of snow, which allows us to assimilate the data with an EnKF [*Su et al.*, 2008]. Our study differs from *Su et al.* [2008] in the finer scale of the assimilated SCF observations and by supplementing the EnKF with a rule-based SCF assimilation algorithm that allows updates when the model simulates completely snow-covered or snow-free conditions.

[6] Some of the above problems with SCF assimilation can be overcome by using passive microwave observations. Sensors like the Scanning Multichannel Microwave Radiometer (SMMR, 1978–1987), the Special Sensor Microwave Imager (SSM/I, 1987 to present) and the Advanced Microwave Scanning Radiometer for the Earth Observing System (AMSR-E, 2002 to present) do not suffer from cloud obscuration and allow SWE estimation by relating the microwave brightness temperature to snow parameters. However, these products typically have a coarser resolution, and a low accuracy [*Foster et al.*, 2005; *Dong et al.*, 2005; *Cordisco et al.*, 2006; *Kelly*, 2009; *Tedesco et al.*, 2010; *Tedesco and Narvekar*, 2010]. Alternatively, active microwave sensors could be explored [*Stankov et al.*, 2008], but the applications have been limited, because of the lack of spaceborne measurements at optimal frequencies (Ku-band). SWE assimilation has been explored in synthetic experiments [*Sun et al.*, 2004; *De Lannoy et al.*, 2010]. A few studies attempted to assimilate SMMR or AMSR-E SWE retrievals, but only with marginal success [*Dong et al.*, 2007; *Andreadis and Lettenmaier*, 2006]. It has been suggested that radiance assimilation may be more effective [*Durand and Margulis*, 2006, 2007; *Andreadis et al.*, 2008; *Durand et al.*, 2009].

[7] A number of blended satellite SWE products have been proposed [*Kongoli et al.*, 2007; *Gao et al.*, 2010; *Foster et al.*, 2011] that merge visible, near-infrared, and passive microwave observations, but most of these products are research products and only generated for a limited time period and area. Improved analyses can be expected by dynamically merging snow products in a data assimilation scheme [*Su et al.*, 2010].

[8] The objective of the present study is to examine the possibilities and limitations of assimilating both fine-scale MODIS SCF and coarse-scale AMSR-E SWE retrievals into the Noah LSM using advanced assimilation techniques. In this context, our paper contributes three key innovations to the snow data assimilation literature. We aim at extracting more information from the remotely sensed data than previous AMSR-E SWE and MODIS snow cover assimilation studies by (1) spatially downscaling the AMSR-E SWE retrievals within the assimilation system to address the mismatch between the coarse-scale observations and the fine-scale model resolution, (2) jointly assimilating AMSR-E SWE and MODIS SCF observations in a distributed, multiscale analysis, and (3) assimilating "scaled" (anomaly) SWE and SCF observations to address climatological biases.

[9] Section 2 describes the experiments, section 3 reviews the observations that are used for assimilation and validation, and section 4 explains the data assimilation techniques. The results are analyzed in section 5.

2. Experiment Setup and Overview

[10] The study area and model setup are identical to those of *De Lannoy et al.* [2010] and are discussed here only briefly. The study domain is an area of approximately 75×100 km^2 in size (bottom left corner: 40.25°N, −106.75°W; upper right corner: 41.00°N, −105.75°W) in Northern Colorado, USA, including a central plain surrounded by mountain chains (Figure 1). This area was part of NASA's Cold Land Processes Experiments (CLPX) to evaluate SWE retrievals from spaceborne passive microwave sensors. Furthermore, this domain includes a substantial area with flat topography and a dense collection of long-term in situ SWE observations for validation.
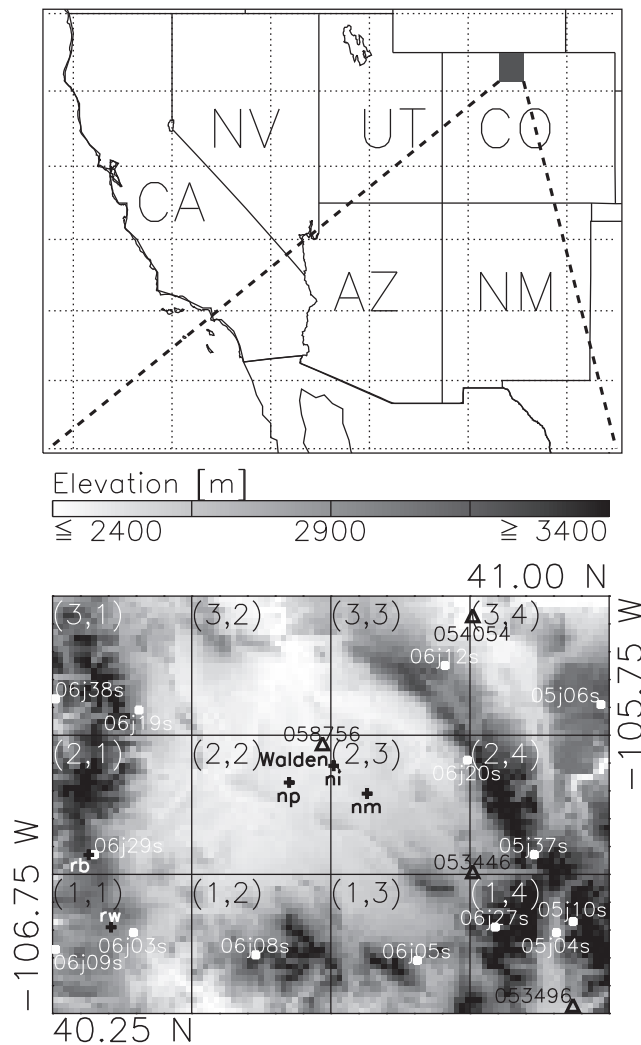
Figure 1. Study domain with the 1 km topography as background, AMSR-E pixel boundaries (25×25 km^2, with indication of pixel coordinates) and in situ observation locations for SNOTEL (dots) and COOP (triangles). The crosses cover 1 km^2 intensive study areas monitored during the NASA Cold Land Processes Experiments for North Park (Illinois River (ni), Michigan River (nm), and Potter Creek (np)) and for Rabbit Ears (Buffalo Pass (rb), Walton Creek (rw)).

[11] The land surface model of the National Centers for Environmental Prediction/Oregon State University/Air Force/Hydrologic Research Lab (Noah, version 2.7.1 [*Ek et al.*, 2003]) is used within the National Aeronautics and Space Administration (NASA) Land Information System version 5.0 (LIS5.0) [*Kumar et al.*, 2006; *Peters-Lidard et al.*, 2007; *Kumar et al.*, 2008], and forced with surface meteorological data from the North American Land Data Assimilation System (NLDAS, see http://ldas.gsfc.nasa. gov/nldas/). All simulations are performed at a 0.01° (∼1 km) resolution (7500 grid cells). Details on Noah snow processes can be found in the work of *Ek et al.* [2003]. Recently, several changes to Noah have been suggested to mitigate the underestimation of modeled SWE and snow

depth [*Barlage et al.*, 2010; *Livneh et al.*, 2010; *Wang et al.*, 2010].

[12] The ensemble simulations are initialized in 1997 to allow 5 years of spin-up of the entire land system before the snow assimilation period from September 2002 through July 2010, covering 8 winter seasons. The forecasted snow state is updated by assimilating fine-scale MODIS SCF observations (daily at 17:00 UTC) and/or coarse-scale AMSR-E SWE observations (daily at 08:00 UTC) using an EnKF. Figure 2 shows a schematic of the experiments. Specifically, we discuss the ensemble open loop without assimilation (EnsOL) and three assimilation experiments: (1) assimilation of coarse-scale AMSR-E SWE observations (SWE DA); (2) assimilation of fine-scale MODIS SCF observations (SCF DA); and (3) joint, multiscale assimilation of AMSR-E SWE and MODIS SCF observations (SWE & SCF DA). The three assimilation experiments are performed either (1) with the unscaled satellite observations, or (2) using the anomaly information in the observations, i.e., after scaling these observations to avoid systematic differences in model and observation climatologies (see section 4.5 for details).

[13] The SWE estimates obtained through assimilation of satellite observations without a priori scaling (experiments 1a, 2a, and 3a) are validated directly against in situ SWE measurements at SNOTEL or COOP sites. When scaled satellite observations are assimilated (experiments 1b, 2b, and 3b), we validate the anomalies from the assimilation against the corresponding anomalies from the in situ measurements, i.e., the data set-specific climatology is subtracted from the in situ data and assimilation results. Note that the direct validation against in situ observations is subject to spatial scaling errors, although this issue is mitigated when anomalies are validated to assess the temporal (interannual) variability of the results (section 4.5).

3. Observations

3.1. AMSR-E SWE

[14] In this study, we assimilate the Aqua AMSR-E Level-3 Daily Snow SWE product (AE_DySno, V09, R. E. Kelly et al., AMSR-E/Aqua daily L3 global snow water equivalent EASE-Grids v009, 2002–2010, see http://nsidc. org/data/ae_dysno.html [*Kelly*, 2009]) provided by the National Snow and Ice Data Center (NSIDC). We resampled the SWE data from a hemispheric 25 km equal area grid to a 0.25° resolution geographic coordinate system. The product only includes descending (nighttime) overpasses. There are 12 (3×4) AMSR-E pixels covering the study area (Figure 1).

[15] The AMSR-E SWE values in our study area and timeframe range from 0 to 240 mm. The maximum SWE value recorded in the global NSIDC product is 480 mm, which occurs only for specific snow classes outside our study domain. Typical error standard deviations for the AMSR-E retrievals range between 10 and 50 mm in terms of SWE, or ∼10–250 mm in terms of snow depth (based on comparison with in situ observations [*Pulliainen and Hallikainen*, 2001; *Kelly et al.*, 2003; *Derksen et al.*, 2003; *Foster et al.*, 2005; *Tedesco and Narvekar*, 2010]). The actual errors depend strongly on the time and location of
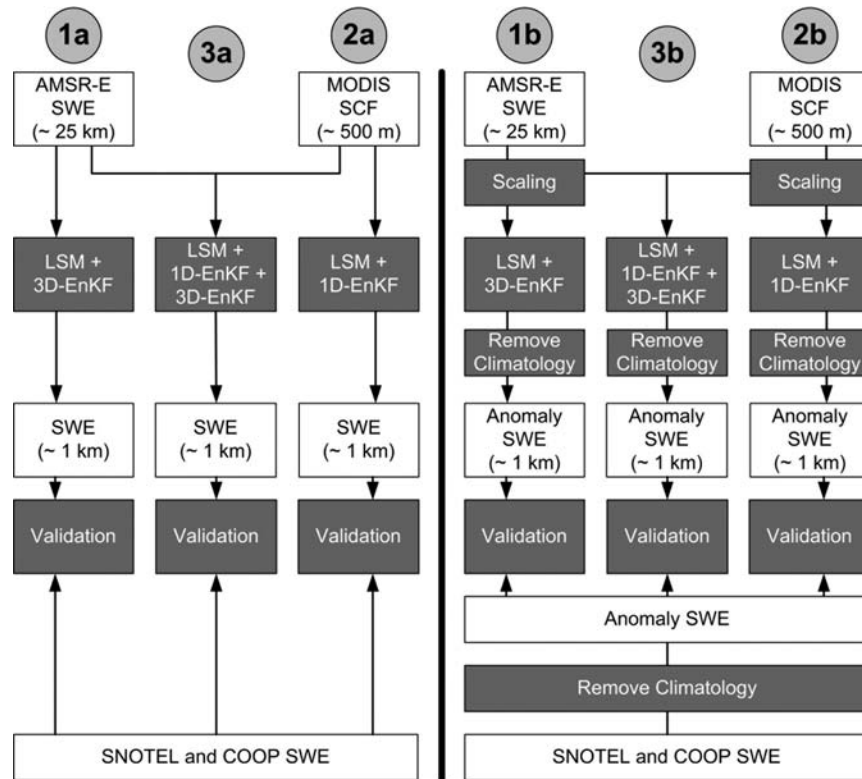
Figure 2. Schematic of the data assimilation experiments: (1a, 1b) AMSR-E SWE assimilation, (2a, 2b) MODIS SCF assimilation, and (3a, 3b) joint AMSR-E SWE and MODIS SCF assimilation. The remote sensing data are either assimilated (1a, 2a, 3a) as they are (without scaling) or (1b, 2b, 3b) after rescaling. If scaled data are assimilated, then the analysis anomalies are compared against in situ anomalies by removing the climatology of each data set.

the individual observations. Locally, errors on the order of 100 mm SWE and higher have been reported [*Tekeli*, 2008; *Tedesco and Narvekar*, 2010], mainly for deeper snowpacks [*Dong et al.*, 2005; *Tong et al.*, 2010].

[16] Figure 3 illustrates typical scaling errors of the AMSR-E SWE estimates versus snowpit SWE values collected during NASA's CLPX [*Cline et al.*, 2004] in early 2003. In the flat, lower-elevation North Park area, AMSR-E SWE exceeds the shallow in situ snow measurements by up to a factor ~5–10, while AMSR-E underestimates SWE in the mountainous, high-elevation Rabbit Ears area by a factor ~10. In other words, the coarse-scale (~25 × 25 km^2) SWE amount across an AMSR-E pixel does not necessarily represent local snow amounts that are measured in the spatially averaged (including up to 16 snowpits) snowpit data scattered across a 1 km^2 area.

[17] A number of detection issues affect passive microwave snowpack estimates. These include the presence of wet snow, open water bodies, metamorphism, complex topography, vegetation interference, and signal saturation [*Kelly et al.*, 2003; *Dong et al.*, 2005] with increasingly uncertain retrievals above 100 mm SWE. Another issue is the assumed constant snow density [*Sturm et al.*, 1995] in the conversion from snow depths to SWE retrievals [*Tedesco and Narvekar*, 2010]. The recently released GlobSnow product (see www.globsnow.info, [*Pulliainen*, 2006]) attempts to better constrain the SWE retrievals in

nonmountainous areas through an optimization of the snow grain size and assimilation of in situ information, but does not (yet) provide coverage over our study domain.
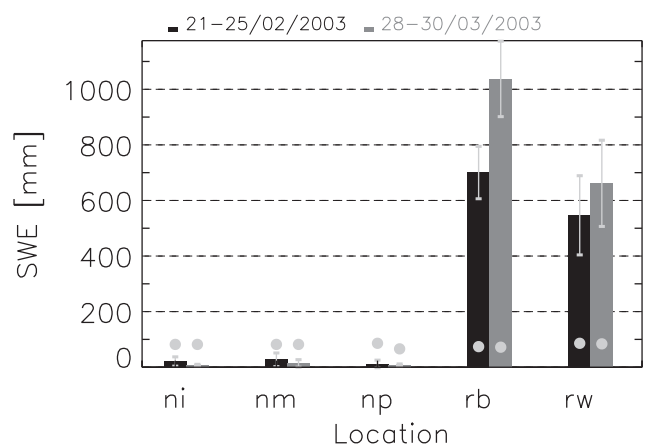

Figure 3. SWE from AMSR-E (dots) retrievals and snowpit measurements (bars) in 5 CLPX intensive study areas (see Figure 1), for 2 periods in 2003: (black) 21 through 25 February, (gray) 28 through 30 March. For each study area, SWE estimates are averages over up to 16 snowpits. Error bars indicate 1 standard deviation across the individual snowpits.

3.2. MODIS SCF

[18] MODIS provides snow cover, albedo and SCF products, including daily 500 m Terra MODIS SCF observations on a sinusoidal grid (MOD10A1–5, D. K. Hall, G. A. Riggs, and V. V. Salomonson, MODIS/Terra snow cover daily L3 global 500m grid V005, 2002–2010, see http://nsidc.org/data/mod10a1v5.html). We regridded these 500 m SCF observations to the 0.01° model grid by averaging SCF only over the cloud-free 500 m pixels within each 0.01° grid cell. MODIS SCF observations from Terra are obtained through an algorithm that uses MODIS bands 4 (0.55 μm) and 6 (1.6 μm) to calculate a Normalized Difference Snow Index (NDSI) [*Hall et al.*, 1998], which is related to the SCF [*Salomonson and Appel*, 2004]. Note that SCF retrievals from MODIS on the Aqua platform use the less optimal band 7 (2.105–2.155 μm) because of a technical problem with that sensor's band 6, which results in less accurate retrievals that are not used here.

[19] The most frequent errors in MODIS SCF observations are related to snow/cloud discrimination (in collection 5, this has been improved through a revised cloud mask), detection of very thin or ephemeral snow (<10 mm) and snow estimation in forested and complex terrain areas [*Hall and Riggs*, 2007].

3.3. In Situ Data

[20] Two sets of in situ measurements are used to validate the satellite, model, and assimilation estimates: (1) SNOTEL SWE observations and (2) COOP snow depth observations. In situ SNOTEL SWE measurements from pressure sensing snow pillows are reported daily at 08:00 UTC and distributed by the US Department of Agriculture NRCS (see http://www.wcc.nrcs.usda.gov/snow/). The COOP snow depth measurements (see http://www.ncdc.noaa.gov) are distributed by the National Climate Data Center as daily measurements at different times throughout the years and over the different stations. For simplicity, we

assume that all COOP observations are taken at 14:00 UTC for validation (which is, on average, the nearest time of day across all observations). For validation purposes, the snow depth measurements are converted to SWE by multiplication with a density of 230 kg m^{-3}, the average snow density for our study area that is used in the AMSR-E SWE retrieval algorithm [*Kelly*, 2009; *Sturm et al.*, 1995]. The details of the 14 SNOTEL and 4 COOP sites with sufficient available data are summarized in Figure 1 and Table 1.

4. Data Assimilation

[21] The data assimilation system used in our study is based on the ensemble Kalman filter (EnKF) [*Reichle et al.*, 2002; *Evensen*, 2003] and is identical to that of *De Lannoy et al.* [2010] unless otherwise indicated here.

4.1. Ensemble Perturbation

[22] Uncertainty is introduced into the ensemble forecast by perturbing select forcing and state variables, using 20 ensemble members. Precipitation (PR) and downward shortwave radiation (SW) are subject to multiplicative perturbations with mean = 1 and standard deviations of 0.5 (PR) and 0.1 (SW), respectively. Moreover, zero-mean, additive perturbations are applied to air temperature (TA) and longwave radiation (LW) with standard deviations of 0.5 K (TA) and 15 W m^{-2} (LW), respectively. The single-layer Noah model prognostic variables for SWE (swe^-) and snow depth (snd^-) are subject to multiplicative perturbations with mean = 1 and standard deviation = 0.01. The TA and state perturbations are intentionally small to avoid systematic differences between the EnsOL run and a deterministic (no perturbation, no assimilation) model integration. All perturbations have spatial correlation lengths of 30 km (larger than the resolution of the coarse-scale observations, *De Lannoy et al.* [2010]), which is needed for the 3-D-EnKF (see below). In addition, we impose cross-correlations ρ between perturbations to state variables

Table 1. Characteristics of In Situ Stations and Select Model Parameters for the Corresponding 1 km^2 Grid Cells[a]

	In Situ Station Characteristics					Model Parameters		
Name	ID	Lon (°E)	Lat (°N)	Elev [m]		Elev [m]	Vegetation Class	*snup* [m]
				SNOTEL				
Willow Creek Pass	06j05s	−106.09	40.35	2907.76		2884	evergreen needleleaf forest	0.04
Arapaho Ridge	06j08s	−106.38	40.35	3340.57		3313	evergreen needleleaf forest	0.04
Rabbit Ears	06j09s	−106.74	40.37	2865.09		2797	bare ground	0.02
Columbine	06j03s	−106.60	40.39	2791.93		2790	grassland	0.02
Phantom Valley	05j04s	−105.85	40.40	2752.31		2760	evergreen needleleaf forest	0.04
Never Summer	06j27s	−105.96	40.40	3133.31		3109	evergreen needleleaf forest	0.04
Lake Irene	05j10s	−105.82	40.41	3261.32		3286	evergreen needleleaf forest	0.04
Joe Wright	05j37s	−105.89	40.53	3084.54		3109	open shrubland	0.02
Tower	06j29s	−106.68	40.54	3200.36		3190	evergreen needleleaf forest	0.04
Rawah	06j20s	−106.01	40.71	2749.26		2927	woodland	0.04
Zirkel	06j19s	−106.60	40.79	2846.80		2868	open shrubland	0.02
Deadman Hill	05j06s	−105.77	40.81	3115.02		3100	evergreen needleleaf forest	0.04
Lost Dog	06j38s	−106.75	40.82	2840.70		2838	evergreen needleleaf forest	0.04
Roach	06j12s	−106.05	40.88	2956.52		2987	evergreen needleleaf forest	0.04
				COOP				
Grand Lake 1 NW	053496	−105.82	40.27	2657.90		2669	evergreen needleleaf forest	0.04
Gould 4se Sfsp	053446	−106.00	40.50	2743.20		2806	evergreen needleleaf forest	0.04
Walden	058756	−106.27	40.73	2455.50		2455	cropland	0.013
Hohnholz Rch	054054	−106.00	40.97	2365.20		2374	grassland	0.02

[a]The vegetation classes are according to the UMD land cover classification.

(ρ (swe^-,snd^-) = 0.9) and forcing fields (ρ (SW,LW) = -0.3; ρ (SW,PR) = -0.5; ρ (SW,TA) = 0.3; ρ (LW,PR) = 0.5; ρ (LW,TA) = 0.6; ρ (PR,TA) = -0.1) (following the approach of *Reichle et al.* [2007]).

4.2. SWE Assimilation and Downscaling

[23] The coarse-scale AMSR-E observations are assimilated using a distributed 3-D-EnKF, specifically method 3D_Cm of *De Lannoy et al.* [2010]. In each fine-scale (1 km) grid cell k, the state vector at one particular time step (time index omitted) is $\hat{x}_k^- = \begin{pmatrix} swe_k^- \\ snd_k^- \end{pmatrix}$. The EnKF is used to update these two model prognostic variables at the fine scale by assimilating multiple (m) coarse-scale observations simultaneously. For an ensemble member j, the a priori state $\hat{x}_k^-$ is updated to $\hat{x}_k^+$ as follows:

$$\hat{x}_k^{j+} = \hat{x}_k^{j-} + K[y^j - \hat{y}^{j-}] \qquad (1)$$

$$K = \text{Cov}[\hat{x}_k^-, \hat{y}^-][\text{Cov}[\hat{y}^-, \hat{y}^-] + R]^{-1}, \qquad (2)$$

where y^j denotes the perturbed AMSR-E observations (m elements), R the observation error covariance, and $\hat{y}^{j-} \equiv h(\hat{x}^{j-})$ is short-hand for the corresponding model predictions of these observations, with $h(\cdot)$ the observation operator. In our study we thus have

$$y^j = \begin{pmatrix} swe_{\kappa_1}^{obs,j} \\ swe_{\kappa_2}^{obs,j} \\ ... \\ swe_{\kappa_m}^{obs,j} \end{pmatrix} \quad \text{and} \quad \hat{y}^{j-} = \begin{pmatrix} 1/625 & \Sigma_{l=1}^{625} swe_{k_{l,1}}^{j-} \\ 1/625 & \Sigma_{l=1}^{625} swe_{k_{l,2}}^{j-} \\ ... \\ 1/625 & \Sigma_{l=1}^{625} swe_{k_{l,m}}^{j-} \end{pmatrix}, \quad (3)$$

where κ_m, $m = 1, 2, ..., N_{obs}$ denotes a coarse-scale grid cell and $k_{l,m}$, $l = 1, 2, ..., 625$ indexes the fine-scale grid cells contained within κ_m. N_{obs} is the number of observed (≤ 12, depending on the swath) coarse-scale AMSR-E pixels in our study domain for the update time step. Through the imposed spatial error correlations (correlation length = 30 km), each fine-scale grid cell senses the impact of surrounding coarse-scale observations, and unobserved areas are updated. The impact decreases for more remote observations and becomes negligible beyond a localization length scale of 75 km. We approximate the observation error standard deviation with a linear function of the SWE amount: $\sqrt{[R]_\kappa} = 5 + 0.2 \cdot swe_\kappa^{obs}$ [mm], reflecting the reported increase in SWE retrieval errors for deeper snowpacks. Note that the model forecast uncertainty also increases for deeper snowpacks [*De Lannoy et al.*, 2010]. As in the work of *Andreadis and Lettenmaier* [2006], we avoid the assimilation of AMSR-E data when either the observed or model-predicted SWE exceeds a snowpack saturation value of 240 mm, but this constraint has almost no effect over our simulation domain, because our snowpacks are generally lower than this threshold.

4.3. SCF Assimilation

[24] Unlike binary information on snow presence, MODIS SCF observations are real numbers based on the NDSI (section 3.2) and can be assimilated with a Kalman

filter [*Su et al.*, 2008, 2010]. The update equation is identical to equation (1), but for SCF we use a 1-D-EnKF, that is, y^j and $\hat{y}^{j-}$ only contain a single fine-scale observation per fine-scale grid cell k and unobserved areas (e.g., cloud covered) are not updated. The (scalar) SCF innovations $[y^j - \hat{y}^{j-}]_k$ are calculated by differencing the (regridded) $0.01°$ MODIS SCF observations (y_k) and the model forecast SCF ($\hat{y}_k^{j-} = scf_k^{j-}$), obtained from the forecasted SWE (swe_k^{j-}) via the snow depletion curve of the Noah LSM, which serves as the observation operator. Specifically, we have

$$\hat{y}_k^{j-} = \begin{cases} 1 - \left[e^{\left(-4 \cdot \frac{swe^{j-}}{snup}\right)} - \frac{swe^{j-}}{snup} \cdot e^{-4} \right]_k, & \text{if } swe_k^{j-} < snup_k \\ 1, & \text{if } swe_k^{j-} >= snup_k \end{cases}, \qquad (4)$$

where swe_k^{j-} and $snup_k$ are in units of m and the predicted $\hat{y}^{j-} = scf_k^{j-}$ is a dimensionless fraction. The parameter $snup$ is a vegetation class–dependent time-invariant SWE threshold above which full coverage is assumed (see Table 1).

[25] Evidently, a simple snow depletion curve with a single vegetation-dependent parameter will not account for all terrain heterogeneity [*Luce et al.*, 1998; *Shamir and Georgakakos*, 2007; *Luce et al.*, 1999]. In an earlier study by *Andreadis and Lettenmaier* [2006], an observation-based curve was used to assimilate MODIS SCF with an EnKF, which can be expected to result in a better performance. *Essery and Pomeroy* [2004] suggested that prognostic schemes may be required to account for the actual snowpack dynamics.

[26] For SCF, the EnKF update equation (1) must be supplemented with a rule-based update. As Figure 4a illustrates, a given perturbation to the swe^- state results in a decreasing spread (uncertainty) in scf^- as swe^- increases. For deep model snowpacks (high swe^- values), the ensemble spread of scf^- is thus very small and the EnKF update cannot reduce the forecasted SWE if only partial coverage is observed. Similarly, the EnKF update cannot induce the onset of snow accumulation in the model forecast if all ensemble members are free of snow, again because there is no spread (uncertainty) in the model ensemble.

[27] These two situations are addressed with a rule-based update. If all forecast ensemble members have a snow cover below an infinitesimal value of $\epsilon = 10^{-6}$ for a given grid cell, and if the observed snow cover scf^{obs} exceeds $\gamma_{scf} = 0.3$, then a nominal amount of 20 mm of water equivalent is added to SWE, and a corresponding 87 mm (assuming a density of 230 kg m^{-3}) are added to snow depth:

$$\text{if} \quad \max_j(scf_k^{j-}) < \epsilon \text{ and } scf_k^{obs,j} > \gamma_{scf} : \begin{cases} swe_k^{j+} = swe_k^{j-} + 20\,\text{mm} \\ snd_k^{j+} = snd_k^{j-} + 87\,\text{mm} \end{cases}. \qquad (5)$$

If all forecast ensemble members essentially have full snow cover and the observed scf_k^{obs} is less than $1 - \gamma_{scf} = 0.7$,
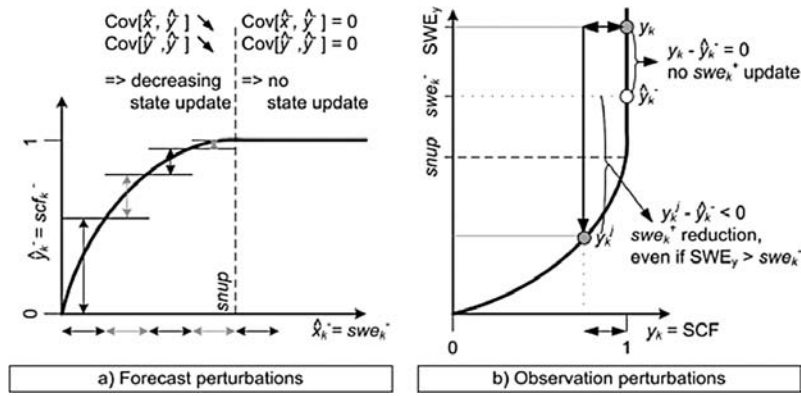
Figure 4. Assimilation of MODIS SCF: (a) with increasing swe^- the spread in scf^- decreases and the assimilation impact decreases, (b) perturbation of observed 100% snow cover (y_k) will decrease the corresponding SWE below $snup$.

then the forecast state variables are reduced to a quarter of their values:

$$\text{if} \quad \min_j(scf_k^{j-}) > 1 - \epsilon \text{ and}$$

$$scf_k^{obs,j} < 1 - \gamma_{scf} : \begin{cases} swe_k^{j+} = swe_k^{j-}/4 \\ snd_k^{j+} = snd_k^{j-}/4 \end{cases}. \qquad (6)$$

Smaller thresholds γ_{scf} allow more impact of SCF observations on the analysis, but may also be problematic. Even under "full" cover, the MODIS observations typically range from 0.95 to 1. Using $\gamma_{scf} < 0.05$ would thus lead to a systematic removal of SWE from the forecast state. The reduction to a quarter of the snow amount is an arbitrary choice, and attempts to weigh the information in the observations more than the forecasts.

[28] Figure 4b shows the effect of perturbing the MODIS SCF observations in the assimilation scheme. Perturbing full snow cover always reduces the observed snow cover, causing the corresponding SWE amount to decrease below the $snup$ value. Consequently, the analysis increment would always be negative, even if there was more snow observed than forecasted (as suggested by $SWE_y > swe_k^-$ in Figure 4b). Thus, SCF assimilation with perturbed observations would systematically and substantially underestimate SWE. This problem can be addressed through careful modeling of the observation error variance. In this study, we use

$$\sqrt{[\mathbf{R}]_k} = \begin{cases} 0.5 \cdot scf_k^{obs}, & \text{if} \quad scf_k^{obs} <= 0.5 \\ 0.5 \cdot (1 - scf_k^{obs}), & \text{if} \quad scf_k^{obs} >= 0.5 \end{cases}, \qquad (7)$$

that is, starting from $\sqrt{[\mathbf{R}]_k} = 0$ at $scf_k^{obs} = 0$, the observation error standard deviation increases linearly to a value of 0.25 at $scf_k^{obs} = 0.5$ and thereafter decreases again, reaching 0 at $scf_k^{obs} = 1$. For SCF near 1, the observation perturbations are thus effectively disabled. In reality, we do not expect the SCF observations to be perfect for zero or full cover. For example, zero cover during the accumulation and melt phase may include subpixel-scale snow patches that happened to be obscured by clouds. More sophisticated observation error models could be explored in future

studies or alternatively, an ensemble square root filter implementation [*Whitaker and Hamill*, 2002] could perhaps be used to avoid the observation perturbations.

4.4. Multi-Scale SWE and SCF Assimilation

[29] Both AMSR-E and MODIS observations are also assimilated jointly by alternating between 3-D-EnKF updates at 08:00 UTC using coarse-scale AMSR-E SWE observations and l-D-EnKF updates at 17:00 UTC using fine-scale MODIS SCF observations. The forecast and observation error specifications are identical to those of the single sensor assimilation experiments, although it can be expected that the forecast error estimates remain smaller with a higher assimilation frequency. Additional tuning of the error parameters could further optimize the joint filter but is left for future studies.

4.5. Anomaly Assimilation

[30] Earlier studies have highlighted different climatologies in different satellite SWE products [*Derksen et al.*, 2003]. Moreover, in situ data generally differ in magnitude from remote sensing products that represent larger areas [*Moser et al.*, 2009] and estimates from land models [*Pan et al.*, 2003; *Mote et al.*, 2003; *Rawlins et al.*, 2007]. The climatological differences present difficulties for satellite data assimilation (the Kalman filter assumes unbiased forecasts and observations) as well as for in situ validation. To sidestep some of these difficulties, *Slater and Clark* [2006] assimilated percentiles of in situ snow observations and *Andreadis and Lettenmaier* [2006] validated percentiles of AMSR-E SWE assimilation results against percentiles of in situ observations.

[31] Here, the 3-D assimilation scheme accounts for some of the spatial scale discrepancy between the assimilated observations and the model, but climatological differences between the model and (assimilated and validation) observations remain at the 25 km and the 1 km scales, as will be shown in the experiments where satellite observations are assimilated without a priori scaling. To address these biases, we repeat all experiments (Figure 2), but this time we assimilate only the anomaly information from the observations by scaling the satellite observations prior to data assimilation as follows.

[32] We calculate for each data set a climatological seasonal cycle of the snowpack evolution by first smoothing the time series with a 30 day window and then averaging the resulting time series over 8 winters. For the data assimilation experiments, the coarse AMSR-E SWE observations are scaled to the 25×25 km^2 EnsOL climatology before assimilation. This scaling approach effectively adjusts the magnitude of the SWE peak climatology, but it does not always correctly scale the timing of onset and melt. The anomalies are not scaled for their variability, because the AMSR-E data are prone to a lot of noise, and tests showed that such a second-order scaling mainly amplified the noise. Likewise, the MODIS SCF observations are scaled to their corresponding 1 km^2 EnsOL climatology.

[33] The scaling of the satellite observations to the model climatology does *not* imply that we trust the model climatology more than that of the observations. Scaling the satellite observations prior to data assimilation as described above is equivalent to assimilating only the anomaly information from the satellite observations. The bias is *not* assigned to the model or the observations, and the climatology (and long-term bias) will be disregarded in the validation. As shown in Figure 2, the departures (anomalies) from the climatological seasonal cycle are calculated for both the assimilation estimates and the in situ validation observation data (SNOTEL/COOP), and then used to validate the skill of the assimilation scheme [*Reichle et al.*, 2010]. The climatological seasonal cycle for the assimilation results and the SNOTEL/COOP sites is again calculated as the 8 year average of the smoothed time series and subtracted from the "raw" data. This operation avoids the representativeness bias in the in situ observations and focuses on the validation of the interannual variations only. Simply put, in high snow years, we expect high positive anomalies in both the in situ observations and the assimilation results, while in low-snow years, negative anomalies should appear in both data sets.

5. Results

5.1. Comparison of Satellite Observations and Model Estimates

[34] Before we assess the assimilation results, we briefly discuss the skill of the satellite retrievals and the model estimates. First, the AMSR-E SWE product is compared to the aggregated EnsOL simulations at the coarse (25 km) resolution. Figure 5a shows that the climatological seasonal SWE cycles for the EnsOL and AMSR-E data are very different in magnitude and shape. Typically, peak SWE amounts are greater and occur earlier for EnsOL than AMSR-E. Figure 5b shows the EnsOL estimates and AMSR-E values in a single, representative coarse-scale pixel over 8 years and Figure 5c shows the corresponding anomaly time series. There is a significant interannual variation in the model simulations, while only very little interannual variability can be found for the otherwise noisy AMSR-E observations. Scaling of the AMSR-E retrievals will remove the long term observation-minus-forecast bias and mostly result in higher SWE values. However, the relative lack of interannual variability (causing short-term bias) limits what can be achieved through assimilation of AMSR-E SWE anomalies. Over 8 winters (October–June 2002–2010) and for the 12 coarse-scale (25 km) pixels, the root-mean-square-difference is RMSD = 64 mm, the mean observed-minus-simulated SWE bias = -23 mm and the correlation is R = 0.25 between the unscaled AMSR-E data and 25 km EnsOL (not shown). For the anomalies, we obtain RMSD = 51 mm, bias = 1 mm (instead of 0 mm, due to resetting rare negative SWE values to 0 mm after rescaling) and R = 0.005 (not shown).

[35] The SCF assimilation is impacted by the Noah snow depletion curve. Figure 6 shows the (1 km) EnsOL and MODIS SCF values for the corresponding EnsOL SWE, averaged over 8 years and over all grid cells in the two dominant vegetation classes. For all vegetation classes (not shown), the observed SCF is generally lower than that of the model for high SWE values, because MODIS rarely ever reports 100% cover. In forested areas, the snow cover is typically underestimated. After scaling, the low observed SCF values for classes with taller vegetation (e.g., forest) are shifted closer to the model climatology (Figure 6(top)). For short vegetation (e.g., grassland), SCF rises quickly with increasing SWE in the model (because of small values for *snup*) and in the observations (because short vegetation does not obscure the signal). Therefore, scaling has a negligible effect in this case (Figure 6(bottom)). For both vegetation classes the mean scaled MODIS SCF never reaches 100%, because all positively anomalous SCF observations are set back to 100% cover when the model climatology for SCF is 100%.

5.2. Effect of Data Assimilation on Spatial Patterns

[36] Figure 7 illustrates the spatial patterns of the satellite observations, the EnsOL estimates, and the assimilation estimates (without scaling) for a few representative days during the winter of 2009–2010, at time steps with limited cloud cover. For this winter, the model and unscaled satellite observations have a similar SWE magnitude. At the start (12 October) and end (31 May) of the snow season, AMSR-E retrievals indicate little if any snow, while MODIS SCF reports snow in the mountains on both dates. The 3D_Cm filter performs a downscaling of the coarse AMSR-E SWE observations and shows a realistic fine-scale variability driven by the land surface model integration. For example, high elevations maintain SWE values well above the observed AMSR-E SWE (e.g., 7 January), which would not be the case if the AMSR-E pixels were a priori disaggregated and assimilated with a 1-D filter. Furthermore, areas without observations (swath effects, e.g., 2 March) are updated through spatial correlations in the forecast errors, which prevents delineations between observed and nonobserved areas.

[37] The 1-D SCF filter imposes the fine-scale MODIS-observed variability on the snowpack, and locations without fine-scale observations (due to clouds) are not updated. SCF assimilation successfully adds snow during accumulation under freezing temperatures (e.g., 18 November, 7 January), but it is more difficult to keep added snow during the snow melt, especially in lower elevation areas, when temperatures are above freezing (e.g., 10 April). The combined SWE and SCF assimilation shows features of both the SWE and SCF assimilation integrations. The spatial (pattern) correlation (versus the in situ measurements, averaged over 8 winters) is generally much smaller for the
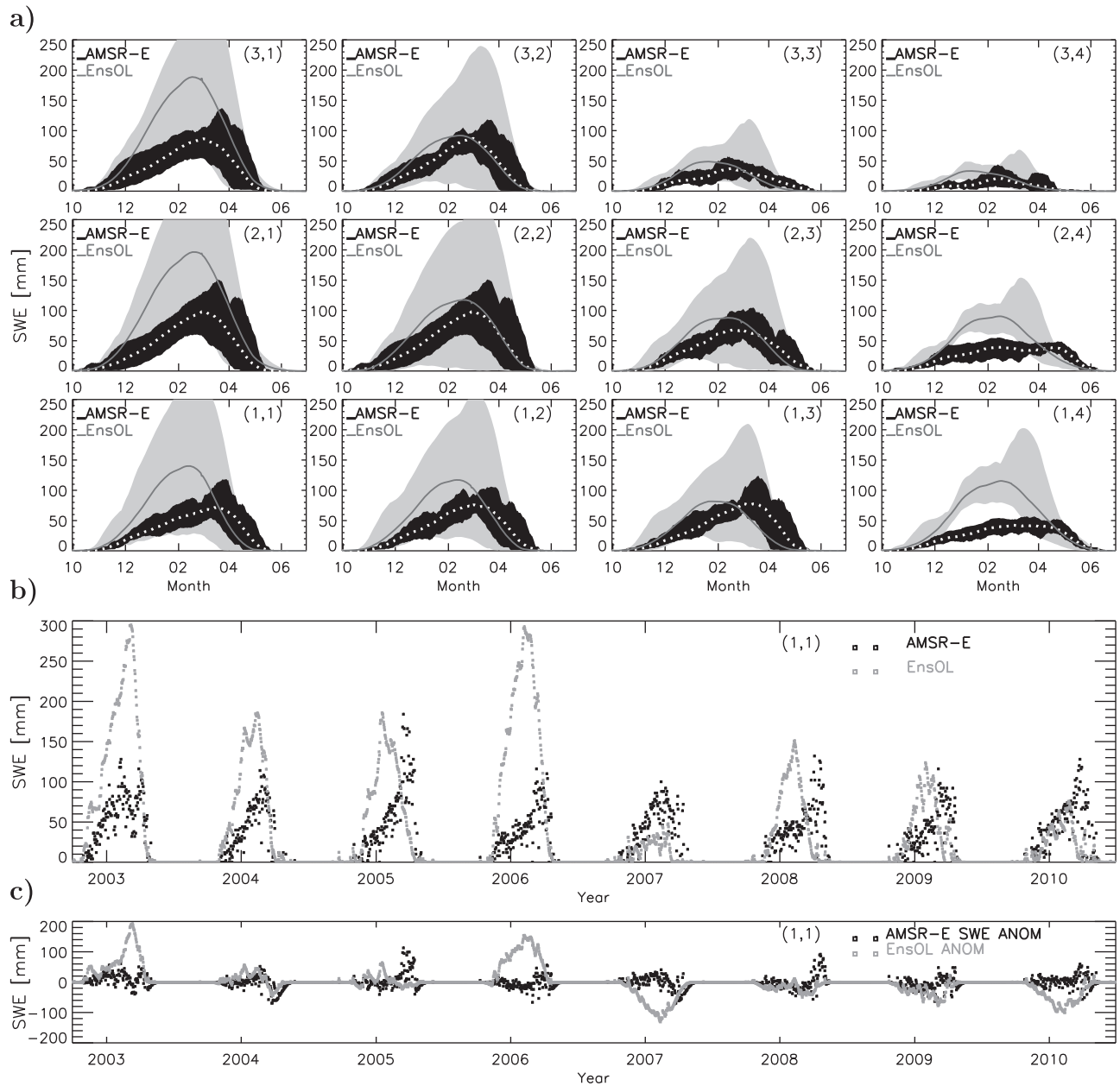
Figure 5. (a) AMSR-E (white dotted line) and Noah (gray solid line) area-averaged 8 year SWE climatology and range between 8 year minimum and maximum values (shaded areas), for each of the 12 (25 × 25 km²) AMSR-E pixels (pixel coordinates as in Figure 1). (b) An example of the 8 year time series for the single coarse pixel (1,1) at the south-western corner of the domain. (c) Corresponding anomaly time series for the same single coarse pixel (1,1).

remote sensing products (R ∼ 0.1 − 0.2 for MODIS-based and AMSR-E SWE) than for the EnsOL model integration (R ∼ 0.5). The assimilation estimates maintain R ∼ 0.5, both without and (not shown in Figure 7) with a priori scaling of the satellite observations.

5.3. Time Series Analysis: Assimilation Without Prior Scaling

[38] Figure 8 shows the time series R values and root-mean-square error (RMSE) values of different assimilation integrations versus in situ observations. The RMSE and R values are computed separately for each in situ sensor and

then averaged over all available sensors. Figures 8a and 8c also show 95% confidence intervals for the average R values. The RMSE and R values only include times and locations where snow is present in both the assimilation estimates and the in situ measurements (i.e., zero snow is excluded), thereby avoiding the consideration of "trivial" skill in the performance metrics during extended snow-free periods. In section 5.6, we analyze timing errors in snow accumulation and melt.

[39] Figures 8a and 8b show the results after assimilating the data without a priori scaling. At the COOP locations with shallow snowpacks, some improvement can be obtained
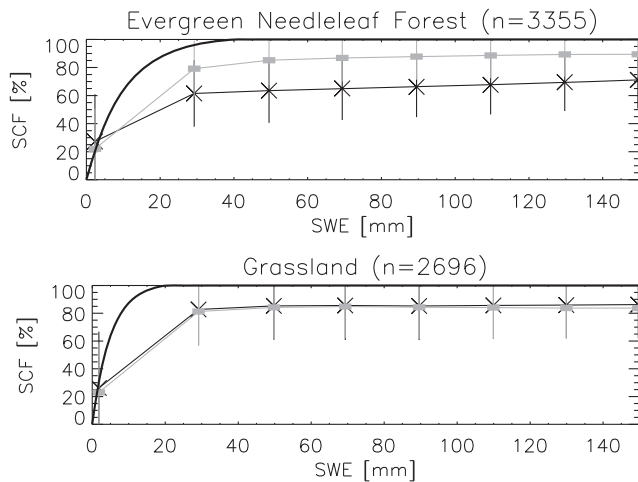
Figure 6. Noah predicted SCF (thick solid line), unscaled (black crosses), and scaled (gray rectangles) MODIS SCF observations. The SCF values are averaged per simulated SWE (EnsOL) bin over all locations within each of the two dominant vegetation classes over 8 years (October–June 2002–2010). The error bars show the spread in SCF values for a particular SWE range across all locations and times. The number n indicates the total amount of 1 km^2 grid cells falling in each vegetation class.

over the EnsOL by assimilating either AMSR-E SWE (Δ R = 0.06) or MODIS SCF (Δ R = 0.04). Closer inspection of the time series shows that the EnsOL has a larger SWE range than the COOP observations, because the model does not account for effects like wind-driven snow redistribution (not shown). The limited range in the AMSR-E SWE nudges the assimilation estimates closer to the observed seasonal cycle for COOP sites. The SCF assimilation also has a positive impact, because the low-snow conditions allow sufficient spread in the ensemble observation predictions (scf^-), which in turn enables frequent EnKF updates. In addition, these sites experience less cloud cover and thus more regular updates. Typically, SCF assimilation contributes most during the transition seasons with patchy or thin snow, while SWE assimilation has more impact for greater snow cover. Consequently, at COOP sites, the modest individual contributions from the SWE and SCF assimilation add up to a significant improvement in the SWE evolution upon joint, multisensor SCF and SWE assimilation (R = 0.21, RMSE = 62 mm) compared to the EnsOL (R = 0.10, RMSE = 78 mm).

[40] However, at the SNOTEL sites, none of the data assimilation scenarios without scaling (R $\sim$ 0.0, RMSE $\sim$ 330 − 350 mm) improves the performance over the EnsOL (R = 0.19, RMSE = 305 mm). Without assimilation, there is a large discrepancy between the EnsOL and the SNOTEL observations, mainly due to their highly elevated location, deep and long-lasting snowpacks, a higher chance for precipitation in the form of snow as compared to rain, the coarser scale of the NLDAS precipitation forcing, and model parameterization. SWE assimilation leads to estimates that are more different from the dynamic SNOTEL observations than the EnsOL estimates: in the deep

snowpack areas around SNOTEL sites (e.g., coarse pixels (1,1), (2,1), (3,1) and (1,4) in Figure 5a), the negative bias in the coarse-scale (25 km) SWE innovations dampens the temporal variability in the analyses. Furthermore, while the downscaling included in the assimilation accounts for the scale difference between the model (1 km) and the SWE retrievals (25 km), the direct validation of the 1 km model (or assimilation) results against the SNOTEL point observations is still prone to scaling errors. The limited skill of SWE assimilation for deeper snowpacks was also noted by *Andreadis and Lettenmaier* [2006] and *Dong et al.* [2007].

[41] The assumed constant snow density in the retrieval of the AMSR-E SWE could adversely affect the results. To avoid this assumption, we also tested the assimilation of AMSR-E snow *depth* retrievals (as opposed to SWE retrievals) but obtained largely similar results. Our conclusions are further supported by experiments with SWE and snow depth retrieval assimilation over the entire Northern Hemisphere [*Kumar et al.*, 2011].

[42] At the SNOTEL sites, SCF assimilation slightly reduces snowpack because of underobserved MODIS snow cover in forest areas and inaccurate conversions from SCF to SWE. The resulting decrease in R (Figure 8a) is also due to irregularities in the spatial and temporal patterns (cloud obscuration; a mix of updated and nonupdated time steps and locations are included in the R calculation). At the SNOTEL sites, the joint SWE and SCF assimilation is dominated by the adverse impact of SWE assimilation and leads to worse estimates than those obtained from the land surface model alone (EnsOL).

5.4. Time Series Analysis: Assimilation With Prior Scaling

[43] In Figures 8c and 8d, we validate the analysis anomalies after assimilating anomaly satellite information (where anomalies are obtained by removing the data set-specific mean seasonal cycle from the time series). The anomaly RMSE values shown in Figure 8d are reduced compared to the values in Figure 8b because the long-term bias is excluded. Again, statistically significant improvements in the anomaly R and RMSE are found for the COOP sites through joint SCF and SWE assimilation (Δ RMSE = −11 mm with respect to the EnsOL). SCF assimilation dominates the positive impact, while SWE assimilation has almost no impact on the synoptic-scale or interannual variability.

[44] At SNOTEL locations, no improvement can be found for either scaled AMSR-E SWE or MODIS SCF assimilation. Figure 9a illustrates several limitations inherent in SWE anomaly data assimilation for the winter of 2009–2010 at one fine-scale SNOTEL location. While the SNOTEL sites all show a late melt in this year (relative to the 8 year climatology), there is no late snow simulated, and the AMSR-E SWE anomalies do not show late snow either (AMSR-E is not sensitive to thin snow layers, and local snow patches are not obvious in coarse-scale measurements). It is thus impossible to introduce late snow anomalies into the analysis through SWE assimilation. Furthermore, during this particular winter, the AMSR-E anomalies are mostly positive while the model and most in situ observed SNOTEL anomalies are primarily negative. Hence the temporal variability in the analysis product is
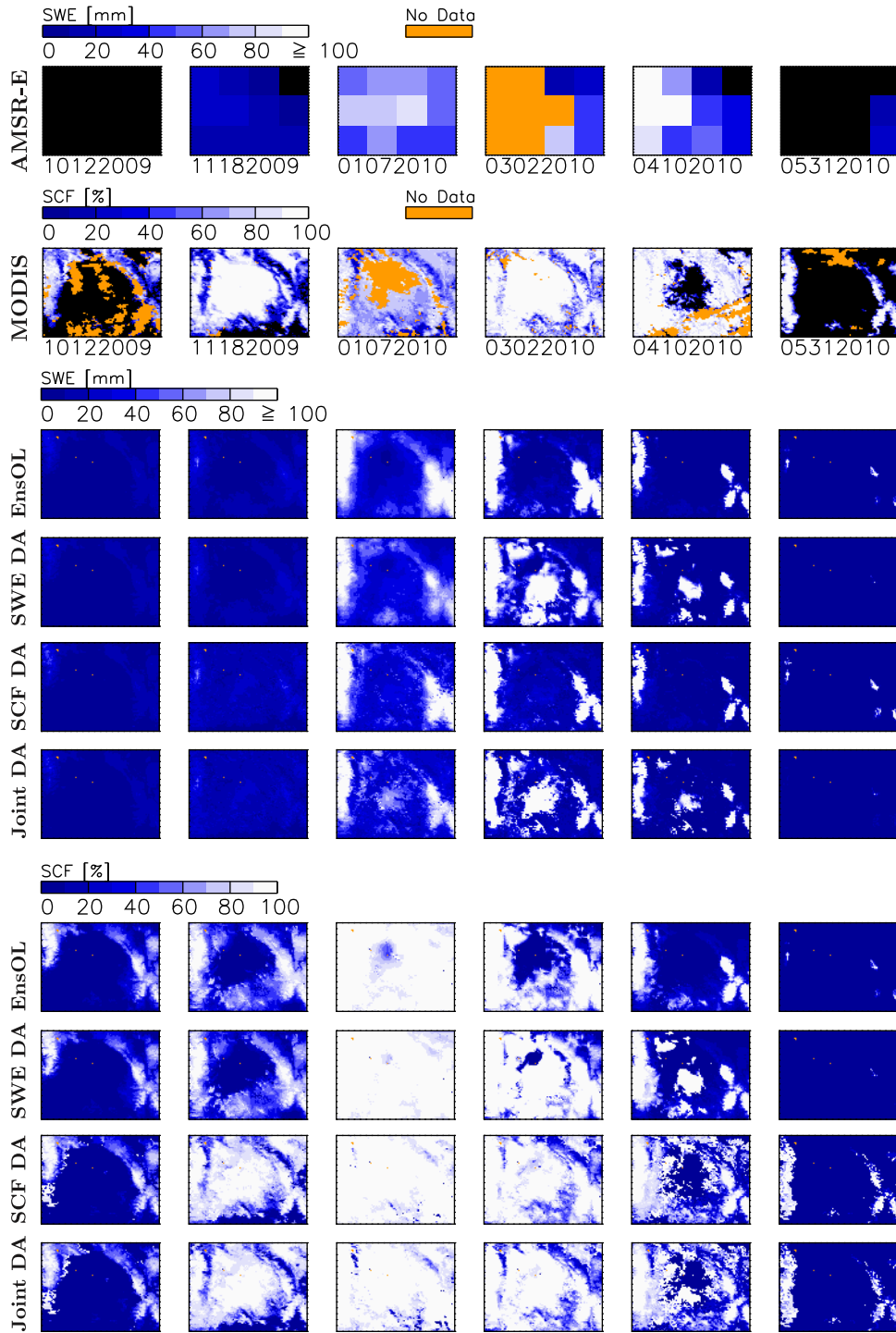
Figure 7. SWE (at 08:00 UTC) and SCF (at 17:00 UTC) fields for 5 days (MMDDYYYY) in the winter of 2009–2010. No snow is indicated as black. The top 2 rows show individual SWE and SCF satellite observations. The remaining rows show SWE (at 09:00 UTC) and SCF (at 18:00 UTC) for the EnsOL forecast and 3 different analyses obtained through data assimilation (DA) without a priori scaling: SWE DA, SCF DA, and joint SWE & SCF DA, respectively. AMSR-E data are missing due to the swath effect and MODIS data are missing because of cloud cover.

deteriorated. This comes as no surprise, because the anomaly correlation between the SNOTEL in situ and AMSR-E observations is close to zero. Scaled SWE assimilation is not successful, because (1) the SWE product lacks a correct

interannual variability, probably as a result of a saturation error in the retrievals and interannually changing snow properties [*Rosenfeld and Grody*, 2000] that affect the brightness temperature signal and (2) the simple bias
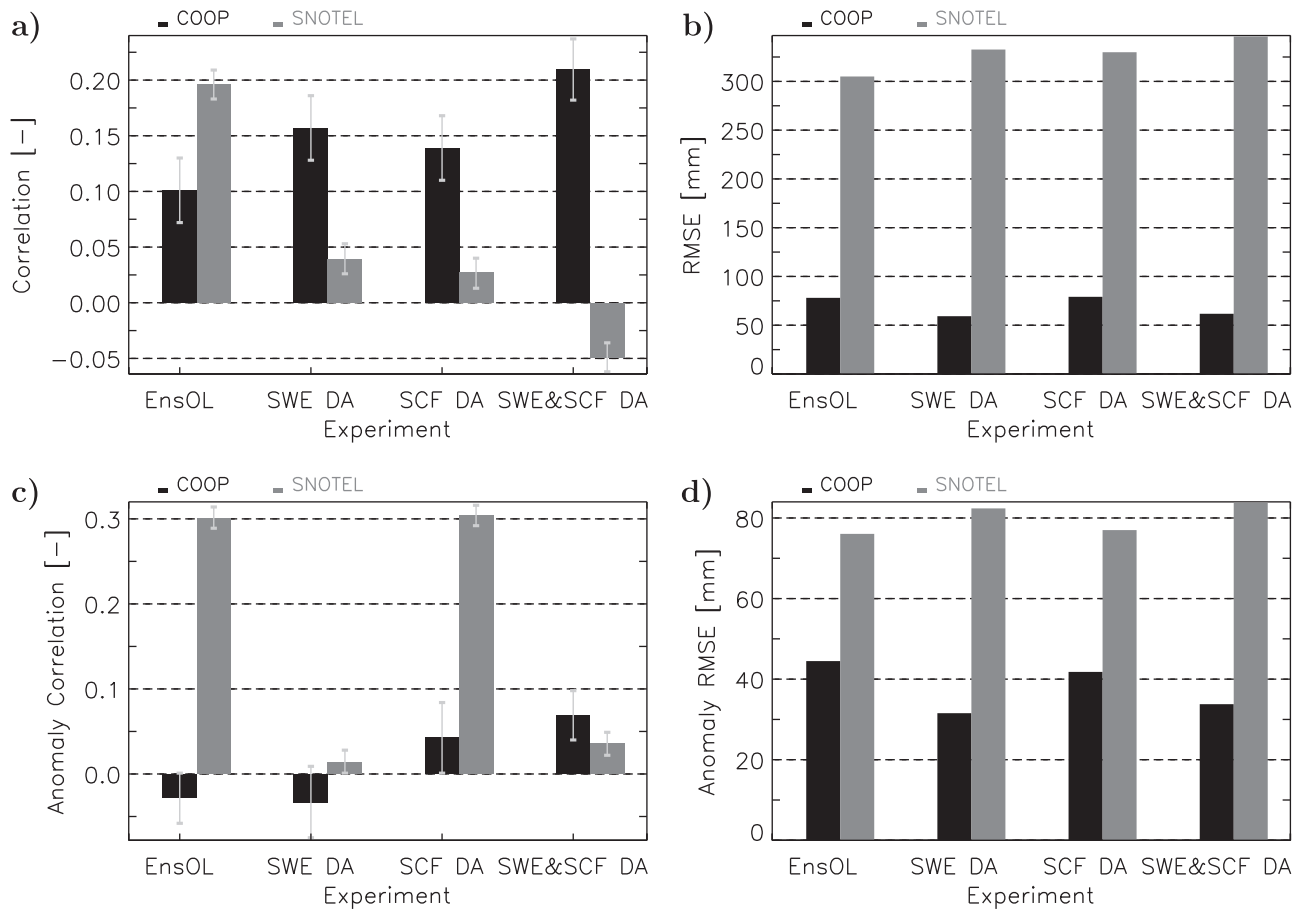
Figure 8. (a) Time series correlation R and (b) RMSE versus in situ observations (COOP (black bars) and SNOTEL (gray bars)) for model forecasts (EnsOL) and assimilation analyses, computed over 8 winters (October–June 2002–2010). (c and d) Same as Figures 8a and 8b but showing anomaly R and anomaly RMSE for assimilation using scaled satellite observations. The average R values are supplemented with 95% confidence intervals.

removal strategy used here cannot correct for interannual variations and fine-scale bias.

[45] Because of their long-lasting deep snow and nearly complete snow cover, the SNOTEL sites are only marginally impacted by scaled MODIS SCF assimilation during the midwinter (Figure 9b). During the melt period, SCF assimilation is unable to add and maintain the snow cover if the model tends to melt the snow (for example, because the model forcing results in above-freezing temperatures). Using future snow observations to adjust the air temperature [*Zaitchik and Rodell*, 2009] may help to solve this problem.

5.5. Water Balance and Increments

[46] The different assimilation scenarios have a distinct impact on the water budget. Table 2 compares the season-average SWE against the corresponding accumulated snowfall minus sublimation and melt (P-S-M), averaged over 8 snow seasons (October through June) and over the entire domain. For the EnsOL without assimilation, both the averaged SWE and P-S-M are approximately balanced at ∼40 mm (Table 2). SWE assimilation without a priori scaling excessively removes SWE (to ∼19 mm) and thus leaves less snow available for melt and sublimation, which increases P-S-M (to ∼69 mm). SCF assimilation without a

priori scaling also reduces the snowpack during the midwinter (to ∼30 mm), but large melt and sublimation events occur when nominal amounts of snow are added in the spring while the model is quickly melting off snow. This results in low average P-S-M (∼20 mm), which is again out of balance with the time-average SWE. Similarly, joint SWE and SCF assimilation without a priori scaling results in a notable water imbalance.

[47] By contrast, scaled data assimilation better preserves the water balance, even though all scenarios still show a slightly reduced snowpack relative to the EnsOL (Table 2). Snow additions and removals (increments) might at first glance be expected to compensate each other. But while snow removal is a linear process, snow additions do not result in a commensurately increased snowpack, because of melt and sublimation. Thus, this nonlinear effect results in a slight reduction in the climatological snowpack. Scaled SCF assimilation again yields a reduced P-S-M because nominal amounts of added snow increase the melt.

[48] The changes in the water balance are directly related to the distribution of the assimilation increments. Note again that for the 3-D SWE assimilation, the increments are always computed for and applied to the entire domain, i.e., also at unobserved locations. Figure 10 shows the long-
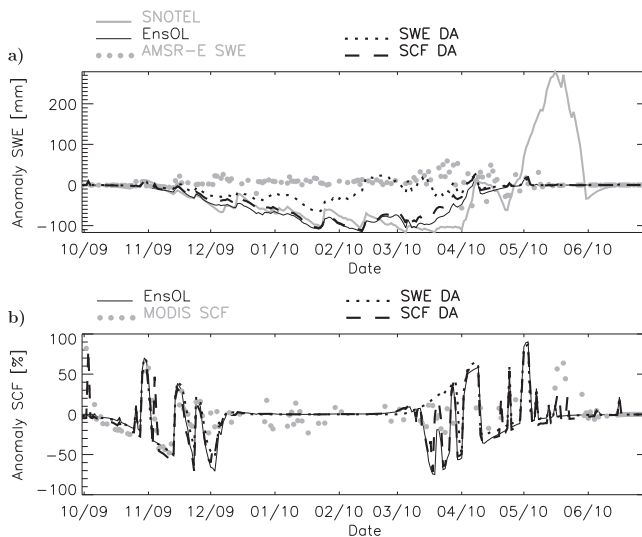
Figure 9. (a) SWE and (b) SCF anomalies during the winter of 2009–2010 at the Columbine SNOTEL site (06j03s). The EnsOL and anomaly assimilation integrations (SWE DA, SCF DA), as well as the validating in situ anomaly observations (SNOTEL) are shown at 07:00 UTC. The SWE and SCF satellite observations are assimilated at 08:00 UTC and 17:00 UTC, respectively. Model and assimilation estimates are at 1 km scale. The date indicates month/year.

term (8 winters) mean and standard deviation of the SWE increments for each 1 km^2 gridcell in the domain, calculated over observed and unobserved time steps for SWE assimilation (Figures 10a and 10b) without prior scaling and (Figures 10c and 10d) with prior scaling. Also shown are the statistics for the spatially averaged increments over each of the 12 (25 × 25 km^2) AMSR-E pixels. In this context, a 1 km^2 gridcell is considered observed for a given update time step if it is covered by an assimilated SWE retrieval at that time. Unobserved increments are obtained through propagation of information from a partially observed (swath) area to unobserved areas. SWE assimilation without scaling results in predominantly negative increments (Figure 10a), and reduces the snowpack

Table 2. Water Balance Variables for the Ensemble Open Loop and Different Assimilation Integrations[a]

	SWE [mm]	P-S-M [mm]
EnsOL	41.6	37.3
Without Prior Scaling		
SWE DA	18.8	69.4
SCF DA	30.2	20.2
SWE & SCF DA	18.2	34.7
With Prior Scaling		
SWE DA	35.8	41.5
SCF DA	37.0	23.1
SWE & SCF DA	35.0	24.9

[a]SWE represents the winter season-average SWE accumulation and P-S-M is the winter season-averaged accumulation of snowfall-sublimation-melt. Both are averaged over 8 winters (October to June 2002–2010) and over the entire simulation domain.

(Table 2). However, there is a large spatial variability in the fine-scale increments with positive increments in the central (lower elevation) area of the domain, where AMSR-E tries to add snow, while the model melts it off (not shown).

[49] With a priori scaling, the mean observed increments are zero across the domain (Figure 10c), by design. However, the mean increment for each coarse-scale AMSR-E area is not exactly zero, because of horizontal information propagation across the pixel boundaries. The fine-scale increments show preferential patterns (not shown), which causes the analysis climatology at the fine scale to be different from the EnsOL. For example, deep snowpacks have a larger ensemble spread and therefore attract larger increments.

[50] As expected, for assimilation without and with a priori scaling, the mean and the standard deviation of the unobserved increments are smaller than those of the observed increments because of the reduced error correlation with increasing distance from the observed area (not shown). When the domain is only partially observed, the swath typically covers either the eastern or the western end of the domain. This leads to updates to the unobserved pixels in the center of the domain while the updates (and their standard deviation) are negligible for the opposite side of the domain. The negative unobserved increments mainly occur when information is propagated from the eastern observed area (with less snow) to the unobserved center west part (with deeper snow). It should be noted that the unobserved increments only take a small fraction of the total increments and the spatial distribution of the total increments (not shown) is very similar to that of the observed increments.

5.6. Timing of Accumulation Onset and End of Melt

[51] The time series metrics in Figure 8 assess skill in the snowpack evolution when snow is present. For several applications, however, the onset of the snow accumulation and the last day of snow cover are important and warrant further investigation. Table 3 gives an overview of the mean absolute difference in days between the in situ observed and the simulated date of the onset of accumulation for different assimilation scenarios without a priori scaling. The table also provides the same metric for the timing of snow melt. The RMSE is calculated for each site individually over the 8 years and then averaged over the 14 (or 4) SNOTEL (or COOP) sites. The snow onset date is defined here as the latest date without any snow preceding a period of continuous snow cover for at least 20 days. Likewise, the snow melt date is defined as the earliest date without any snow following a period of continuous snow cover for a period of at least 20 days. For the MODIS and AMSR-E observations, the additional requirement is that less than 5 out of these 20 days can contain missing (and thus potentially zero snow) data. Because of the missing data, the time difference in the onset and melt as observed by the satellite data is an inaccurate estimate. AMSR-E snow typically starts to accumulate later (2 weeks to 1 month) and melt earlier (∼2 months) than the in situ observations, because thin or patchy snow is not observed at the coarse scale.
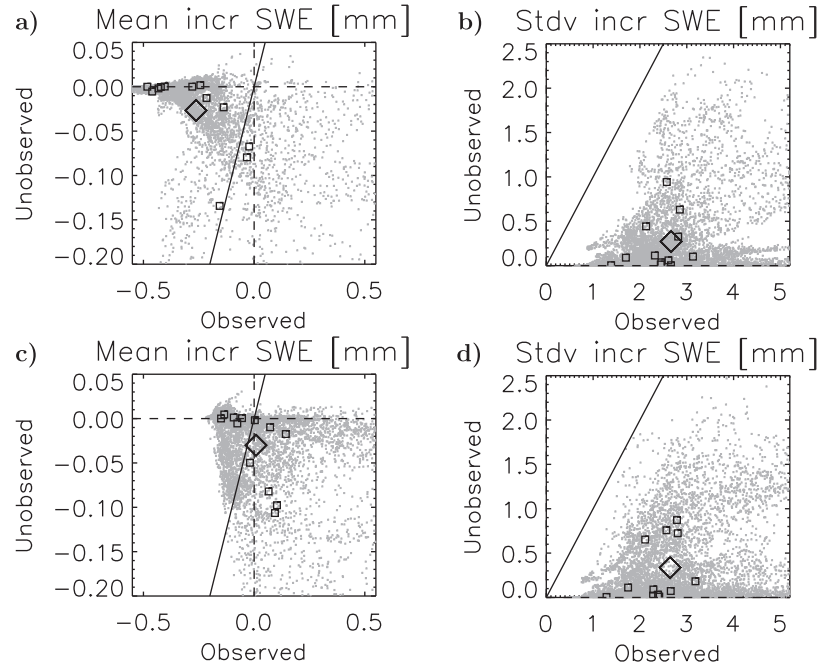
Figure 10. (a and c) Long-term (8 snow seasons) mean and (b and d) standard deviation in daily SWE increments for (gray dots) 1 km^2 pixels in the simulation domain, averaged over each of the 12 AMSR-E pixels (black squares), and averaged over the domain (diamond). Increments were obtained through AMSR-E SWE assimilation (a and b) without and (c and d) with a priori scaling. Each 1 km^2 pixel is observed on average at 1730 time steps, and unobserved (but updated by a neighboring observed area) at 449 time steps. Also shown is the 1–1 line.

[52] SWE assimilation has only a minor impact on the timing of the accumulation onset when compared to the EnsOL, because the modeled onset is maintained, even when snow is reduced by assimilation of zero SWE (snow is never entirely removed in the EnKF analysis, because of assumed errors in the assimilated AMSR-E SWE). Assimilation of unscaled AMSR-E SWE causes an overall reduction in SWE during the midwinter (low-biased SWE) and spring (unobserved thin or patchy snow), which accelerates the ablation and causes a larger error in the analysis timing of the melt than the EnsOL.

[53] SCF assimilation always has a beneficial effect on the snow onset timing estimate and is mostly induced through the rule-based update. However, SCF assimilation is often unable to add and maintain snow (if observed at SNOTEL sites with long-lasting snow cover) once the model starts the snow melt. The joint SWE & SCF assimilation reduces the error in the timing of the onset from 19 (COOP) and 13 (SNOTEL) days to 15 and 9 days, respectively. Less impact of data assimilation can be expected with models that better simulate the exact length of the snow season.

6. Summary and Conclusions

[54] Accurate snowpack estimates are an important part of assessing the land surface water and energy budget. Satellite observations provide estimates of snow cover and snow water equivalent, but with several limitations. In this paper we use advanced ensemble Kalman filter (EnKF) techniques to assimilate the remote sensing retrieval

products from AMSR-E and MODIS into the Noah LSM. The assimilation estimates are validated against in situ SNOTEL and COOP observations.

[55] First, the state-of-the-art techniques for single-sensor snow data assimilation are improved over previous attempts. The coarse-scale AMSR-E SWE retrievals are dynamically downscaled to the finer model scale to limit bias due to the spatial scale mismatch, and information is propagated from observed to unobserved areas through a spatial 3-D-EnKF. High-resolution MODIS SCF observations are assimilated with a 1-D-EnKF. Here the mapping from observed SCF to unobserved snowpack variables (SWE and snow depth) is the main challenge. Both in the absence of snow and in times of full snow cover, the model ensemble of observation predictions will not show any spread, thereby preventing meaningful EnKF updates if the

Table 3. RMSE Between In Situ and Simulated Snow Onset and Snow Melt Dates for 8 Years, Averaged Over Individual Sites[a]

	COOP		SNOTEL	
	Onset	Melt	Onset	Melt
EnsOL	19	60	13	38
AMSR-E	31	98	14	59
MODIS	31	34	35	34
SWE DA	19	71	12	39
SCF DA	17	68	9	39
SWE & SCF DA	15	72	9	40

[a]Data assimilation (DA) is without a priori scaling. RMSE is in days. The 8 years represented are October to June 2002–2010.

SCF observations contradict the model estimates. Therefore, additional rule-based updates have been introduced.

[56] Second, motivated by expected coarse-scale (25 km) climatology bias between simulated SWE predictions and AMSR-E SWE retrievals as well as fine-scale (1 km) bias between the model estimates and in situ validation data, we conduct all experiments without and with scaling of the satellite observations prior to data assimilation. The assimilation of scaled data is essentially anomaly assimilation and validated by comparing SWE departures from the climatological cycle in the in situ observations and the assimilation estimates. This technique thus seeks to assimilate the year-to-year and synoptic-scale SWE (or SCF) variations in the AMSR-E SWE (or MODIS SCF) retrievals, rather than their absolute SWE (or SCF) amounts.

[57] Finally, both AMSR-E SWE and MODIS SCF are assimilated jointly in a multiscale framework. These experiments attempt to overcome shortcomings in each observation type. The coarse-scale AMSR-E SWE does not report thin patchy snow during the transition seasons, but it provides a snow estimate under cloudy conditions. In contrast, fine-scale MODIS SCF observations capture snow during the early accumulation and melt phase, but they do not provide a direct snowpack measurement and are not available when the land surface is obscured by clouds.

[58] Without assimilation, the ensemble open loop integration (EnsOL) shows realistic spatial SWE patterns. Both AMSR-E SWE and MODIS SCF assimilation maintain good spatial patterns in the analyses. For AMSR-E assimilation, this is attributed to the spatial downscaling of the coarse-scale observations in the 3-D-EnKF used here. At shallow snowpack (COOP) locations, assimilation of unscaled AMSR-E SWE brings the seasonal SWE cycle closer to that of the in situ observations. Furthermore, less cloud cover and the low (partial cover) SCF conditions allow more impact of SCF assimilation at the low-elevation stations. Joint SWE and SCF assimilation further improves the results at the COOP sites with significantly enhanced RMSE and R metrics versus in situ observations. Scaled SWE assimilation does not improve the results at COOP sites, but scaled SCF is beneficial and joint scaled SCF and SWE assimilation again has a positive impact.

[59] In areas with deep snowpacks (SNOTEL), AMSR-E SWE assimilation without a priori scaling suffers from climatological biases between the AMSR-E and modeled SWE. Furthermore, underobserved SCF during the midwinter and the imperfect conversion to SWE negatively affect unscaled SCF assimilation results, and scaled SCF assimilation only has a marginal effect in the transition seasons. Furthermore, AMSR-E retrieval assimilation with a priori scaling is not successful, because the SWE product lacks a correct interannual variability and the applied simple bias removal strategy cannot correct for interannual variations and fine-scale bias.

[60] There is a modest benefit at both SNOTEL and COOP sites from SCF assimilation in an improved timing of the onset of the snow season. Yet, SCF assimilation does not improve the melt time estimate, because once the model starts to melt the snow, SCF assimilation is unable to maintain the snowpack. Because AMSR-E SWE retrievals cannot detect thin snow cover or patchy snow conditions, their assimilation does not improve the timing of snow onset or

melt. In fact, SWE assimilation without a priori scaling generates snow melt earlier in the season because the snowpack is typically reduced during the midwinter (due to the low bias in AMSR-E SWE), which increases the difference between the melt times of the assimilation estimates versus those of the in situ observations.

[61] The different assimilation scenarios have a distinct impact on the water balance. Without a prior scaling of the assimilated data, the snowpacks are generally reduced and SWE assimilation causes a reduced melt and sublimation, while SCF assimilation increases the melt. This distortion of the water balance can be largely overcome through scaling of the observations prior to data assimilation.

[62] The assimilation and validation of snow remote sensing products poses several challenges that require further study. MODIS SCF assimilation is impacted by the conversion of SCF to SWE information. Furthermore, while snow removal is mostly effective, any addition of snow only persists if the temperature is below freezing point. The latter issue could be addressed by including a nudging factor to the meteorological forcings [*Zaitchik and Rodell*, 2009]. Problems with AMSR-E snow data assimilation could be further mitigated by (1) improving the retrievals (e.g., using data assimilation within the retrieval process, [*Tedesco et al.*, 2010; *Pulliainen*, 2006]), (2) assimilating radiances directly [*Durand et al.*, 2009] and/or (3) expanding the assimilation scheme with a more complex dynamic bias estimation [*Dee and da Silva*, 1998; *De Lannoy et al.*, 2007], which would need to be state and environment dependent (e.g., different for deep and shallow snowpacks). Unfortunately, SWE estimation is complicated in mountainous areas, but this is exactly where snow matters for water supply. In order to contribute significantly to a data assimilation system, the observations need to reflect realistic synoptic-scale and interannual (spatial and temporal) variations.

[63] In summary, AMSR-E or MODIS snow observations alone come with a number of limitations, and joint snow cover and snowpack data assimilation may have potential to complementary overcome these limitations, as shown here for the COOP sites. However, future improvements for deep snow conditions depend on further advances in assimilation methods and an improved characterization of the synoptic scale (spatial and temporal) variations in the observations.

References

Andreadis, K. M., and D. P. Lettenmaier (2006), Assimilating remotely sensed snow observation into a macroscale hydrology model, *Adv. Water Resour.*, *29*, 872–886.

Andreadis, K. M., D. Liang, L. Tsang, D. P. Lettenmaier, and E. G. Josberger (2008), Characterization of errors in a coupled snow hydrology microwave emission model, *J. Hydrometeorol.*, *9*, 149–164.

Bamzai, A. S., and J. Shukla (1999), Relation between Eurasian snow cover, snow depth, and the Indian summer monsoon: An observational study, *J. Clim.*, *12*, 3117–3132.

Barlage, M., F. Chen, M. Tewari, K. Ikeda, D. Gochis, J. Dudhia, R. Rasmussen, B. Livneh, M. Ek, and K. Mitchell (2010), Noah land surface model modifications to improve snowpack prediction in the Colorado Rocky Mountains, *J. Geophys. Res.*, *115*, D22101, doi:10.1029/2009JD013470.

Barnett, T. P., et al. (2008), Human-induced changes in the hydrology of the Western United States, *Science*, *319*, 1080–1083, doi:10.1126/science.1152538.

Barrett, A. (2003), National operational hydrologic remote sensing center snow data assimilation system (SNODAS) products at NSIDC, *Tech. Rep. NSIDC Spec. Rep. 11*, 19 pp., Nat. Snow and Ice Data Cent., Boulder, Colo.

Brasnett, B. (1999), A global analysis of snow depth for numerical weather prediction, *J. Appl. Meteorol.*, *38*, 726–740.

Brown, R., and P. Mote (2009), The response of northern hemisphere snow cover to a changing climate, *J. Clim.*, *22*, 2124–2145.

Brown, R., and D. Robinson (2011), Northern Hemisphere spring snow cover variability and change over 1922–2010 including an assessment of uncertainty, *Cryosphere*, *5*, 219–229, doi:10.5194/tc-5-219-2011.

Brown, R., C. Derksen, and L. Wang (2010), A multi-data set analysis of variability and change in Arctic spring snow cover extent, 1967–2008, *J. Geophys. Res.*, *115*, D16111, doi:10.1029/2010JD013975.

Clark, M. P., A. G. Slater, A. P. Barrett, L. E. Hay, G. J. McCabe, B. Rajagopalan, and G. H. Leavesley (2006), Assimilation of snow covered area information into hydrologic and land-surface models, *Adv. Water Resour.*, *29*, 1209–1221.

Cline, D., R. Armstrong, R. Davis, K. Elder, and G. Liston (2004), CLPX-ground: ISA snow pit measurements, version 2, edited by M. Parsons and M. J. Brodzik, Nat. Snow and Ice Data Cent., Boulder, Colo.

Cohen, J., and D. Entekhabi (1999), Eurasian snow cover variability and Northern Hemisphere climate predictability, *Geophys. Res. Lett.*, *26*, 345–348.

Cordisco, A., C. Prigent, and F. Aires (2006), Snow characterization at a global scale with passive microwave satellite observations, *J. Geophys. Res.*, *111*, D19102, doi:10.1029/2005JD006773.

Dee, D. P., and A. M. da Silva (1998), Data assimilation in the presence of forecast bias, *Q. J. R. Meteorol. Soc.*, *124*, 269–295.

De Lannoy, G. J. M., R. H. Reichle, P. R. Houser, V. R. N. Pauwels, and N. E. C. Verhoest (2007), Correcting for forecast bias in soil moisture assimilation with the ensemble Kalman filter, *Water Resour. Res.*, *43*, W09410, doi:10.1029/2006WR005449.

De Lannoy, G. J. M., R. H. Reichle, P. R. Houser, K. R. Arsenault, N. E. C. Verhoest, and V. R. N. Pauwels (2010), Satellite-scale snow water equivalent assimilation into a high-resolution land surface model, *J. Hydrometeorol.*, *11*(2), 352–369, doi:10.1175/2009JHM1192.1.

Derksen, C. A., A. Walker, E. LeDrew, and B. Goodison (2003), Combining SMMR and SMM/I data for time series analysis of central North American snow water equivalent, *J. Hydrometeorol.*, *4*, 304–316.

Déry, S. J., and E. F. Wood (2006), Analysis of snow in the 20th and 21st century Geophysical Fluid Dynamics Laboratory coupled climate model simulations, *J. Geophys. Res.*, *111*, D19113, doi:10.1029/2005JD006920.

Déry, S. J., V. V. Salomonson, M. Stieglitz, D. K. Hall, and I. Appel (2005), An approach to using snow areal depletion curves inferred from MODIS and its application to land surface modelling in Alaska, *Hydrol. Processes*, *19*, 2755–2774.

Dong, J., J. P. Walker, and P. R. Houser (2005), Factors affecting remotely sensed snow water equivalent uncertainty, *Remote Sens. Environ.*, *97*, 68–82.

Dong, J., J. P. Walker, P. R. Houser, and C. Sun (2007), Scanning multi-channel microwave radiometer snow water equivalent assimilation, *J. Geophys. Res.*, *112*, D07108, doi:10.1029/2006JD007209.

Drusch, M., D. Vasiljevic, and P. Viterbo (2004), ECMWFs global snow analysis: Assessment and revision based on satellite observations, *J. Appl. Meteorol.*, *43*, 1282–1294.

Durand, M., and S. A. Margulis (2006), Feasibility test of multifrequency radiometric data assimilation to estimate snow water equivalent, *J. Hydrometeorol.*, *7*, 443–457.

Durand, M., and S. A. Margulis (2007), Correcting first-order errors in snow water equivalent estimates using a multifrequency, multiscale radiometric data assimilation scheme, *J. Geophys. Res.*, *112*, D13121, doi:10.1029/2006JD008067.

Durand, M., N. Molotch, and S. A. Margulis (2008a), A Bayesian approach to snow water equivalent reconstruction, *J. Geophys. Res.*, *113*, D20117, doi:10.1029/2008JD009894.

Durand, M., N. Molotch, and S. A. Margulis (2008b), Merging complementary remote sensing datasets in the context of snow water equivalent, *Remote Sens. Environ.*, *112*, 1212–1225.

Durand, M., E. Kim, and S. A. Margulis (2009), Radiance assimilation shows promise for snowpack characterization, *Geophys. Res. Lett.*, *36*, L02503, doi:10.1029/2008GL035214.

Dutra, E., G. Balsamo, P. Viterbo, P. M. A. Miranda, A. Beljaars, C. Schär, and K. Elder (2010), An improved snow scheme for the ECMWF land surface model: Description and offline validation, *J. Hydrometeorol.*, *11*, 899–916.

Dyer, J. (2008), Snow depth and streamflow relationships in large North American watersheds, *J. Geophys. Res.*, *113*, D18113, doi:10.1029/2008JD010031.

Ek, M., K. Mitchell, L. Yin, P. Rogers, P. Grunmann, V. Koren, G. Gayno, and J. D. Tarpley (2003), Implementation of Noah land surface model advances in the NCEP operational mesoscale Eta model, *J. Geophys. Res.*, *108*(D22), 8851, doi:10.1029/2002JD003296.

Essery, R., and J. Pomeroy (2004), Implications of spatial distributions of snow mass and melt rate for snow-cover depletion: Theoretical considerations, *Ann. Glaciol.*, *38*, 261–265.

Evensen, G. (2003), The ensemble Kalman filter: Theoretical formulation and practical implementation, *Ocean Dyn.*, *53*, 343–367.

Foster, J. L., C. Sun, J. P. Walker, R. Kelly, A. Chang, J. Dong, and H. Powell (2005), Quantifying the uncertainty in passive microwave snow water equivalent observations, *Remote Sens. Environ.*, *92*(2), 187–203.

Foster, J. L., et al. (2011), A blended global snow product using visible, passive microwave and scatterometer satellite data, *Int. J. Remote Sens.*, *32*(5), 1371–1395, doi:10.1080/01431160903548013.

Gao, Y., H. Xie, N. Lu, T. Yao, and T. Liang (2010), Toward advanced daily cloud-free snow cover and snow water equivalent products from Terra-Aqua MODIS and Aqua AMSR-E measurements, *J. Hydrol.*, *385*, 23–35.

Gong, G., D. Entekhabi, J. Cohen, and D. Robinson (2004), Sensitivity of atmospheric response to modeled snow anomaly characteristics, *J. Geophys. Res.*, *109*, D06107, doi:10.1029/2003JD004160.

Hall, D. K., and G. A. Riggs (2007), Accuracy assessment of the MODIS snow products, *Hydrol. Process.*, *21*, 1534–1547.

Hall, D. K., J. L. Foster, D. L. Verbyla, A. G. Klein, and C. S. Benson (1998), Assessment of snow cover mapping accuracy in a variety of vegetation cover densities in central Alaska, *Remote Sens. Environ.*, *66*, 129–137.

Hall, D. K., G. A. Riggs, J. L. Foster, and S. V. Kumar (2010), Development and evaluation of a cloud-gap-filled MODIS daily snow-cover product, *Remote Sens. Environ.*, *114*, 496–503.

Jin, J., and N. L. Miller (2007), Analysis of the impact of snow on daily weather variability in mountainous regions using MM5, *J. Hydrometeorol.*, *8*, 245–258.

Kelly, R. E. (2009), The AMSR-E snow depth algorithm: Description and initial results, *J. Remote Sens. Soc. Jpn*, *29*(1), 307–317.

Kelly, R. E., A. T. Chang, L. Tsang, and J. L. Foster (2003), A prototype AMSR-E global snow area and snow depth algorithm, *IEEE Trans. Geosci. Remote Sens.*, *41*(2), 230–242.

Kongoli, C., C. Dean, S. Helfrich, and R. Ferraro (2007), Evaluating the potential of a blended passive microwave-interactive multi-sensor product for improved mapping of snow cover and estimations of snow water equivalent, *Hydrol. Processes*, *21*, 1597–1607.

Kumar, S. V., et al. (2006), Land Information System: An interoperable framework for high resolution land surface modeling, *Environ. Modell. Software*, *21*, 1402–1415.

Kumar, S. V., R. H. Reichle, C. D. Peters-Lidard, R. D. Koster, X. Zhan, W. T. Crow, J. B. Eylander, and P. R. Houser (2008), A land surface data assimilation framework using the Land Information System: description and applications, *Adv. Water Resour.*, *31*, 1419–1432.

Kumar, S. V., R. Reichle, M. Shaw, C. Peters-Lidard, G. D. Lannoy, D. Hall, J. Foster, G. Riggs, and J. Eylander (2011), Assimilation of multi-sensor snow observations into Noah LSM, European Geosciences Union meeting, Geophys. Res. Abstracts, Vienna, Austria.

Lee, S., A. G. Klein, and T. M. Over (2005), A comparison of MODIS and NOHRSC snow-cover products for simulating streamflow using the snowmelt runoff model, *Hydrol. Processes*, *19*, 2951–2972.

Liston, G., and C. A. Hiemstra (2008), A simple data assimilation system for complex snow distributions (SnowAssim), *J. Hydrometeorol.*, *9*, 989–1004.

Liston, G., R. Pielke, and E. Greene (1999), Improving first-order snow-related deficiencies in a regional cimate model, *J. Geophys. Res.*, *104*(D16), 19,559–19,567, doi:10.1029/1999JD900055.

Livneh, B., Y. Xia, K. E. Mitchell, M. Ek, and D. Lettenmaier (2010), Noah LSM snow model diagnostics and enhancements, *J. Hydrometeorol.*, *11*, 721–738, doi:10.1175/2009JHM1174.1.

Luce, C., D. Tarboton, and K. Cooley (1998), The influence of the spatial distribution of snow on basin-averaged snowmelt, *Hydrol. Processes*, *12*, 1671–1683.

Luce, C., D. Tarboton, and K. Cooley (1999), Sub-grid parameterization of snow distribution for an energy and mass balance snow model, *Hydrol. Processes*, *13*, 1921–1933.

Molotch, N. P. (2009), Reconstructing snow water equivalent in the Rio Grande headwaters using remotely sensed snow cover data and a spatially distributed snowmelt model, *J. Hydrometeorol.*, *23*, 1076–1089.

Moser, C. L., O. Aziz, G. A. Tootle, V. Lakshmi, and G. Kerr (2009), A comparison of SNOTEL and AMSR-E snow water equivalent datasets in Western U.S. watersheds, *Cryosphere*, *3*, 32–38.

Mote, P. W., A. F. Hamlet, M. P. Clark, and D. P. Lettenmaier (2005), Declining mountain snowpack in western North America, *Bull. Am. Meteorol. Soc.*, *9*, 1416–1426.

Mote, T. L., A. J. Grundstein, D. J. Leathers, and D. A. Robinson (2003), A comparison of modeled, remotely sensed, and measured snow water equivalent in the northern Great Plains, *Water Resour. Res.*, *39*(8), 1209, doi:10.1029/2002WR001782.

Pan, M., et al. (2003), Snow process modeling in the North American Land Data Assimilation System (NLDAS): 2. Evaluation of model simulated snow water equivalent, *J. Geophys. Res.*, *108*(D22), 8850, doi:10.1029/2003JD003994.

Perry, C. A. (2000), Significant floods in the United States during the 20th century–USGS measures a century of flood, *USGS Fact Sheet 024-00*, U.S. Geol. Surv., Lawrence, Kans. [Available at http://ks.water.usgs.gov/pubs/fact-sheets/fs.024-00.html.]

Peters-Lidard, C. D., et al. (2007), High-performance earth system modeling with NASA/GSFC's Land Information System, *Innovations Syst. Software Eng.*, *3*, 157–165.

Pulliainen, J. (2006), Mapping of snow water equivalent and snow depth in boreal and sub-arctic zones by assimilating space-borne microwave radiometer data and ground-based observations, *Remote Sens. Environ.*, *101*, 257–269.

Pulliainen, J. T., and M. Hallikainen (2001), Retrieval of regional snow water equivalent from spaceborne passive microwave observations, *Remote Sens. Environ.*, *75*, 76–85.

Rawlins, M. A., M. Fahnestock, S. Frolking, and C. J. Vörösmarty (2007), On the evaluation of snow water equivalent estimates over the terrestrial Arctic drainage basin, *Hydrol. Processes*, *21*, 1616–1623.

Reichle, R. H., D. B. McLaughlin, and D. Entekhabi (2002), Hydrologic data assimilation with the ensemble Kalman filter, *Mon. Weather Rev.*, *130*(1), 103–114.

Reichle, R. H., R. Koster, P. Liu, S. P. P. Mahanama, E. G. Njoku, and M. Owe (2007), Comparison and assimilation of global soil moisture retrievals from the Advanced Microwave Scanning Radiometer for the Earth Observing System (AMSR-E) and the Scanning Multichannel Microwave Radiometer (SMMR), *J. Geophys. Res.*, *112*, D09108, doi:10.1029/2006JD008033.

Reichle, R. H., S. V. Kumar, S. P. P. Mahanama, R. D. Koster, and Q. Liu (2010), Assimilation of satellite-derived skin temperature observations into land surface models, *J. Hydrometeorol.*, *11*, 1103–1122.

Rodell, M., and P. R. Houser (2004), Updating a land surface model with MODIS-derived snow cover, *J. Hydrometeorol.*, *5*(6), 1064–1075.

Rosenfeld, S., and N. Grody (2000), Metamorphic signature of snow revealed in SSM/I measurements, *IEEE Trans. Geosci. Remote Sens.*, *38*, 53–63.

Rutter, N., et al. (2009), Evaluation of forest snow processes models (SnowMIP2), *J. Geophys. Res.*, *114*, D06111, doi:10.1029/2008JD011063.

Salomonson, V. V., and I. Appel (2004), Estimating fractional snow cover from MODIS using the normalized difference snow index, *Remote Sens. Environ.*, *89*, 351–360.

Shamir, E., and K. Georgakakos (2007), Estimating snow depletion curves for American river basins using distributed snow modeling, *J. Hydrol.*, *334*, 162–173.

Slater, A. G., and M. Clark (2006), Snow data assimilation via an ensemble Kalman filter, *J. Hydrometeorol.*, *7*, 478–493.

Slater, A. G., et al. (2001), The representation of snow in land surface schemes: Results from PILPS 2(d), *J. Hydrometeorol.*, *2*(1), 7–25.

Stankov, B. B., D. W. Cline, B. L. Weber, and A. J. Gasiewski (2008), High-resolution airborne polarimetric microwave imaging of snow cover during the NASA Cold Land Processes Experiment, *IEEE Trans. Geosci. Remote Sens.*, *46*(11), 3672–3693.

Sturm, M., J. Holmgren, and G. E. Liston (1995), A seasonal snow cover classification system for local to regional applications, *J. Clim.*, *8*, 1261–1283.

Su, H., Z. Yang, G. Niu, and R. E. Dickinson (2008), Enhancing the estimation of continental-scale snow water equivalent by assimilating MODIS snow cover with the ensemble Kalman filter, *J. Geophys. Res.*, *113*, D08120, doi:10.1029/2007JD009232.

Su, H., Z. Yang, R. E. Dickinson, C. R. Wilson, and G.-Y. Niu (2010), Multisensor snow data assimilation at continental scale: the value of Gravity Recovery and Climate Experiment terrestial water storage information, *J. Geophys. Res.*, *115*, D10104, doi:10.1029/2009JD013035.

Sun, C., J. P. Walker, and P. R. Houser (2004), A methodology for snow data assimilation in a land surface model, *J. Geophys. Res.*, *109*, D08108, doi:10.1029/2003JD003765.

Tedesco, M., and P. S. Narvekar (2010), Assessment of the NASA AMSR-E SWE product, *IEEE J. Sel. Top. Appl. Earth Obs. Remote Sens.*, *3*, 141–159.

Tedesco, M., R. Reichle, A. Löw, T. Markus, and J. L. Foster (2010), Dynamic approaches for snow depth retrieval from spaceborne microwave brightness temperature, *IEEE Trans. Geosci. Remote Sens.*, *48*(4), 1955–1967.

Tekeli, A. E. (2008), Early findings in comparison of AMSR-E/Aqua L3 global snow water equivalent EASE-grids data with in situ observations for Eastern Turkey, *Hydrol. Processes*, *22*, 2737–2747.

Tong, J. J., S. J. Dery, P. L. Jackson, and C. Derksen (2010), Testing snow water equivalent retrieval algorithms for passive microwave remote sensing in an alpine watershed of western Canada, *Can. J. Remote Sens.*, *36*, S74–S86.

Wang, Z., X. Zeng, and M. Decker (2010), Improving snow processes in the Noah land model, *J. Geophys. Res.*, *115*, D20108, doi:10.1029/2009JD013761.

Whitaker, J. S., and T. Hamill (2002), Ensemble data assimilation without perturbed observations, *Mon. Weather Rev.*, *130*, 1913–1924.

Yang, F., A. Kumar, W. Wang, H. H. Juang, and M. Kanamitsu (2001), Snow-albedo feedback and seasonal climate variability over North America, *J. Clim.*, *14*, 4245–4248.

Zaitchik, B. F., and M. Rodell (2009), Forward-looking assimilation of MODIS-derived snow-covered area into a land surface model, *J. Hydrometeorol.*, *10*, 130–148.

K. R. Arsenault and P. R. Houser, Department of Atmospheric, Oceanic and Earth Sciences, George Mason University, 4041 Powder Mill Road, Suite 302, MD 20705-3106, Calverton, USA

G. J. M. De Lannoy, V. R. N. Pauwels, and N. E. C. Verhoest, Laboratory of Hydrology and Water Management, Ghent University, Coupure links 653, B-9000 Ghent, Belgium. (gabrielle.delannoy@ugent.be)

S. Kumar, NASA Goddard Space Flight Center, Code 614.3, Greenbelt Road, MD 20771, Greenbelt, USA.

R. H. Reichle, NASA Goddard Space Flight Center, Code 610.1, Greenbelt Road, MD 20771, Greenbelt, USA.